Available online at www.sciencedirect.com
ScienceDirect
Trans. Nonferrous Met. Soc. China 29(2019) 1465−1475
Transactions of Nonferrous Metals Society of China
www.tnmsc.cn

Slip deformation mechanism of α-Zr at 700 °C

Qing-hui ZENG, Adrien CHAPUIS, Bai-feng LUAN, Qing LIU

College of Materials Science and Engineering, Chongqing University, Chongqing 400044, China

Received 12 September 2018; accepted 30 April 2019

Abstract: Mechanical properties, corrosion behavior and hydrogen absorption of zirconium alloys are related to the texture resulting from prior forming processes. In order to investigate the high temperature deformation behavior of α-Zr, compression tests at 700 °C, microstructure measurements via EBSD, and visco−plastic self-consistent modeling were performed. Twinning activity was negligible at strain rates $\dot{\varepsilon} \leq 1\ s^{-1}$. The strain rate sensitivity m=0.17 seemed to be the same for all slip modes. Material parameters were fitted to reproduce the mechanical anisotropy and deformed texture, and were validated by comparing the simulated and measured strain anisotropy. The best-fit simulation showed that at high temperatures prismatic slip was the easiest deformation mode and pyramidal $\langle c+a \rangle$ was the hardest, but basal slip and pyramidal $\langle a \rangle$ slip operated easily and in large amount.

Key words: deformation mechanism; Zr alloy; EBSD; crystal plasticity; plastic deformation

1 Introduction

Zr alloys are widely used in nuclear reactors because of their excellent mechanical properties, good corrosion resistance and low neutron absorption. Because of their hexagonal close-packed (HCP) structure and easy prismatic slip, strong texture forms during the fabrication process. The properties are strongly texture-dependent [1]. Hot rolling or extrusion in a temperature range of 600−850 °C is widely employed in the convoluted processing routes of zirconium components, which can improve the texture of the component effectively [2]. Therefore, it is necessary to investigate the deformation mechanisms of Zr alloys at high temperatures above 600 °C. The understanding and modeling of texture formation are still the subject of many researches. The textures developed in Zr are very similar to those in Ti because the deformation mechanisms are close. $\{10\bar{1}0\}\langle 11\bar{2}0\rangle$ prismatic slip is the most easy deformation mode in these two metals [3,4]. In Zr or its alloys, $\{0001\}\langle 11\bar{2}0\rangle$ basal slip [5,6], $\{10\bar{1}1\}\langle 11\bar{2}0\rangle$ pyramidal $\langle a \rangle$ slip [7] and $\{10\bar{1}1\}\langle 11\bar{2}3\rangle$ pyramidal $\langle c+a \rangle$ slip [8,9], have been observed. Several tension and compression twin modes are activated, mainly at low temperatures [9].

At low temperature, from liquid nitrogen to ambient, basal slip has not been observed in pure Zr single crystals [5]; so early modeling work did not include basal slip when pure Zr deformation was modeled at room temperature (RT) [10] and moderate temperature [11]. Actually, at RT, basal slip was not activated in pure Zr deformed at low strain [12], but was found to be activated at high strain [13], which suggests that the critical resolved shear stress (CRSS) for basal slip is slightly higher than that for pyramidal $\langle c+a \rangle$ slip. In commercially pure Zr, GONG et al [14] measured the CRSS for basal slip to be ~14% more than the CRSS for prismatic slip (which was 206 MPa due to high content of impurities), whereas the CRSS for pyramidal $\langle c+a \rangle$ slip was 2.8 times more than that for prismatic slip.

Moreover, at high temperature basal slip is easily activated in pure Zr. AKHTAR [5] observed basal slip in pure Zr single crystals above 577 °C. At 700 °C, he reported its CRSS to be τ_0^{basal} ~4 MPa and the CRSS for prismatic slip τ_0^{prism} ~2.5 MPa. In polycrystalline pure Zr, KNEZEVIC et al [12] estimated CRSS to be close to that for prismatic slip above 600 °C, and the initial CRSS values were close to those measured on single crystals.

By contrast, basal slip was relatively easily activated at RT in Zircaloy-2 alloy [6], with a CRSS lower than that for pyramidal $\langle c+a \rangle$ slip. Interestingly,

Foundation item: Projects (51531005, 51421001, 51371202, 51505046) supported by the National Natural Science Foundation of China; Project (106112017CDJQJ138803) supported by the Fundamental Research Funds for the Central University of China

Corresponding author: Adrien CHAPUIS, E-mail: achapuis@cqu.edu.cn; Bai-feng LUAN, E-mail: bfluan@cqu.edu.cn

DOI: 10.1016/S1003-6326(19)65053-3

the CRSS ratio for prismatic: basal: pyramidal ⟨*c*+*a*⟩ estimated by QIAO et al [6] was very close to that used to model pure Ti deformation at RT [15].

At moderate temperature, various relative CRSS values have been used. To investigate the deformation of Zircaloy-4 at 550 °C, EVANS et al [16] used roughly the same CRSS for three slip modes (prismatic, pyramidal ⟨*c*+*a*⟩ and basal). Their investigations focused on twinning, but they clearly failed to reproduce the plastic anisotropy and the deformed texture. To model the deformation of Zircaloy-4 at 500 °C, HONNIBAL et al [17] used the same CRSS for prismatic slip and basal slip, whereas the CRSS for pyramidal ⟨*c*+*a*⟩ slip $\tau_c^{\langle c+a\rangle}$ was to be 10 times higher to reproduce the plastic anisotropy and to explain the grain break-up.

The CRSS values for all slip and twinning modes are critical inputs in crystal plasticity models in order to accurately predict the deformation behavior. The previous review showed that the CRSS values strongly depend not only on the temperature and alloying elements, but also on the grain size. Consequently, in order to predict the deformation behavior of Zr alloys at a given temperature, CRSS values should first be fitted. For HCP alloys in which several slip and twinning modes are activated, several experimental data are necessary to accurately fit the model. It is clear that the more the data are, the more accurate the parameters are. However, the visco−plastic self-consistent (VPSC) model has shown great predictability even when parameters are fitted with few experimental data [6,10−13].

At high temperature, deformation is accommodated by slip and small amount of grain boundary sliding [18]. Dynamic recrystallization (DRX) also happens, but recrystallization does not significantly change the deformed texture in HCP metals [19−23]. Most of the time, recrystallized grains have the same orientation as the deformed ones, and texture change involves the prismatic plane distribution whereas the ⟨*c*⟩ axis distribution remains relatively unchanged [22]. In other words, the growth of nuclei can be accompanied by a 30° rotation of the matrix about its basal normal in Zr [17,24]. A similar tendency is observed in Ti, except that texture change is caused by preferential growth of recrystallized grains [20].

Neither recrystallization nor grain boundary sliding can be prevented using crystal plasticity models. For example, to model the plastic deformation behavior of AZ31 Mg alloy, WALDE and RIEDEL [25] implemented a DRX scheme in the VPSC model [26] and simulated hot compression and rolling of Mg alloy AZ31. In the DRX scheme, recrystallized grains inherited the orientation of their parent grains. KIM et al [27] used their own visco− plastic model that included DRX at high temperature. In their model, the recrystallized grains were assumed to have the same crystallographic orientation and volume fraction as their parent grains, and their dislocation density was set to be 0, so that newly recrystallized grains were simply considered as undeformed grains. Consequently, simple crystal plasticity models can be used to simulate the texture evolution of Zr alloys, even at high temperature and when recrystallization happens.

The DRX of Zr alloys deformed at high temperatures has been widely studied [28−30]. Moreover, it has been verified that the DRX mechanisms depend on the deformation mechanisms [31,32]. However, compared with that at low and room temperatures, few studies focus on the deformation mechanisms at high temperatures in Zr alloys. Thus, the present investigation aims to model the deformation of *α*-Zr alloy at 700 °C, using uniaxial compression curves to fit different possible material parameters whereas the deformed textures and plastic anisotropy are used to validate the best material parameters. The standard version of the VPSC, which does not take recrystallyzation into account, is used.

2 Experimental

2.1 Materials and testing

A hot-rolled and annealed Zr−1.06Sn−0.36Nb−0.3Fe−0.1Cr−0.13O (in wt.%) alloy plate was used in this study. In order to investigate the deformation mechanisms of this Zr alloy plate, compression tests were carried out along two different directions of the plate, i.e., normal direction (ND) and transverse direction (TD). Cylindrical compression samples (6 mm × 6 mm) were machined from the plate, with their compression axes parallel to ND or TD. Hereafter, samples are simply named according to their compression direction. The compression tests were carried out in vacuum at 700 °C and four strain rates of 0.001, 0.1, 1 and 10 s^{-1} using a Gleeble 3500 thermal mechanical physical simulation system. Tantalum sheet was used as a lubricant on the surfaces in contact. After compression, the deformed samples were immediately quenched into water to freeze the deformed microstructure. Microstructures were investigated via electron backscatter diffraction (EBSD) subsequently. Samples were sectioned vertically along the compression direction (CD) and observations were made at the middle of the CD−RD (rolling direction of the initial plate) surface. Surface preparation included standard mechanical polishing and electro-polishing with a solution of 10% perchloric acid, 20% 2-butoxy ethanol and 70% methanol. Observations were carried out using a fully automated EBSD system (Oxford Instruments) equipped on a field emission gun scanning electron microscope (Tescan Mira 3−XMU).

The initial microstructure and texture are shown in Fig. 1. The microstructure comprises inhomogeneous grains with average size of 6 μm, measured by circle equivalent diameter with Channel 5, but with many grains between 10 and 20 μm; and a typical bimodal texture with ⟨*c*⟩ close to ND formed and tilted toward TD, without preferential orientation of the prismatic plane.

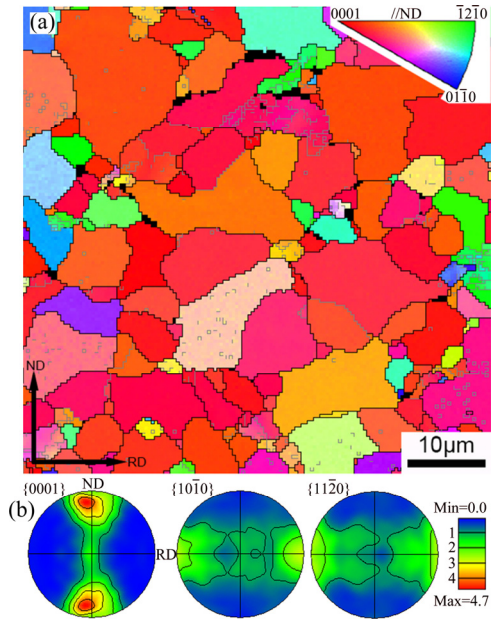

Fig. 1 EBSD inverse pole figure (IPF) map of initial microstructure (a) and associated texture used for simulation (b)

2.2 Modeling procedure

The VPSC model developed by LEBENSOHN and TOMÉ [26] was used to simulate the plastic deformation of Zr at high temperature. In this section, only a brief description of the model is given for definition and notation. Details can be found in Ref. [26].

The Affine self-consistent scheme was often chosen because of its best overall performance at room temperature to model the deformation behavior of Zr [6] and Mg alloys [33]. In the present investigation, the Tangent scheme was also used because its lower stiffness and larger strain incompatibility could be compensated at high temperature by diffusion and grain boundary sliding (phenomena were not taken into account in the model). The Secant scheme, close to the Taylor model, was also considered. These two self consistent schemes constitute respectively the lower- and upper-bound approximation of the material behavior. They will be used to evaluate the reliability of the simulation. The plastic deformation is assumed to be accommodated by prismatic ($\{10\bar{1}0\}\langle 11\bar{2}0\rangle$), basal ($\{0001\}\langle 11\bar{2}0\rangle$), pyramidal ⟨*a*⟩ ($\{10\bar{1}1\}\langle 11\bar{2}0\rangle$), and pyramidal ⟨*c*+*a*⟩ ($\{10\bar{1}1\}\langle 11\bar{2}3\rangle$) slips, which are observed at high temperature [3−8]. Twinning is taken into account in the model, but the observed twin volume fraction at such a high temperature is very low, so twinning is not considered in the present study.

The strain rate tensor $\dot{\varepsilon}$ is computed according to the following equation:

$$\dot{\varepsilon} = \sum_{\alpha} \dot{\gamma}_0 \boldsymbol{P}^{\alpha} \left(\frac{\boldsymbol{P}^{\alpha} : \boldsymbol{\sigma}}{\tau_{\mathrm{c}}^{\alpha}} \right)^{n} \tag{1}$$

where P^{α}, $\dot{\gamma}_0$, $\tau_{\mathrm{c}}^{\alpha}$, n and σ are the Schmid tensor of slip system α, a reference shear rate ($\dot{\gamma}_0$=1 s^{-1}), the CRSS for system α, the strain rate exponent and the stress tensor, respectively. It is important to note that, when the real strain rate exponent is used, the experimental strain rate is put in this strain rate tensor for VPSC simulation.

The CRSS of each deformation mode follows Eq. (2), in which τ_0^{α}, τ_1^{α}, θ_0^{α} and θ_1^{α} constitute the material parameters to be determined:

$$\tau_c^{\alpha} = \tau_0^{\alpha} + (\tau_1^{\alpha} + \theta_1^{\alpha} \Gamma) \left[1 - \exp\left(-\frac{\theta_0^{\alpha}}{\tau_1^{\alpha}} \Gamma \right) \right] \tag{2}$$

where τ_0^{α}, θ_0^{α}, θ_1^{α}, $\tau_0^{\alpha} + \tau_1^{\alpha}$ and Γ are the initial CRSS, initial hardening rate, asymptotic hardening rate, back-extrapolated CRSS and the accumulated shear strain in the grain, respectively. Self and latent hardening parameters are all set to be 1 because of the limited number of available experimental data, and a simplification is generally done when they are undistinguishable.

Simulation was performed with an initial texture containing 2000 grain orientations representative of the initial material, whose pole figure is displayed in Fig. 1.

3 Experimental results

3.1 Strain rate sensitivity

Compression experiments have been done at different strain rates, so the experimental strain rate sensitivity can be computed. Figure 2 shows the true stress−true strain curves for the ND and TD samples at different strain rates. The strain rate sensitivity parameter m ($m = \ln(\sigma_1 / \sigma_2) / \ln(\dot{\varepsilon}_1 / \dot{\varepsilon}_2) = 1/n$) was computed using the ND and TD compression curves at 700 °C and strain rates of 10, 1, 0.1 and 0.001 s^{-1}, and the lowest strain rate increment was considered, so that $\ln(\dot{\varepsilon}_1 / \dot{\varepsilon}_2)$=ln(0.1) or ln(0.01). Figure 3 shows that the strain rate sensitivity parameter depends on the strain rate, the strain, and the sample orientation (or loading direction). However, for $\dot{\varepsilon} \leq 1$ s^{-1}, m=0.16−0.2 is relatively constant, whereas the strain rate sensitivity is much lower for $\dot{\varepsilon}$=10 s^{-1}. The TD sample deformed at $\dot{\varepsilon}$=0.1 s^{-1} experienced precocious softening in comparison to the ones deformed at other strain rates,

which makes the calculated strain rate sensitivities diverge at high strains.

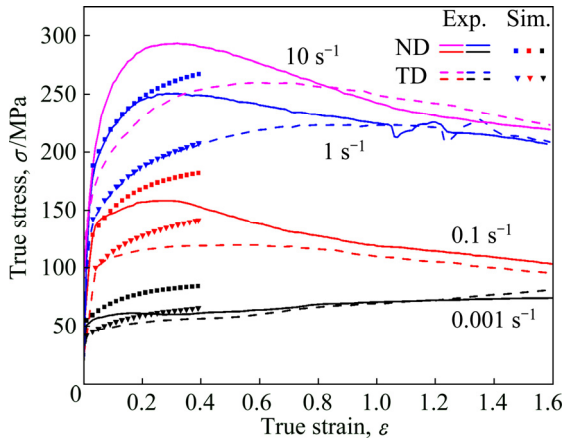

Fig. 2 True stress−true strain curves of TD and ND compressed samples at different strain rates

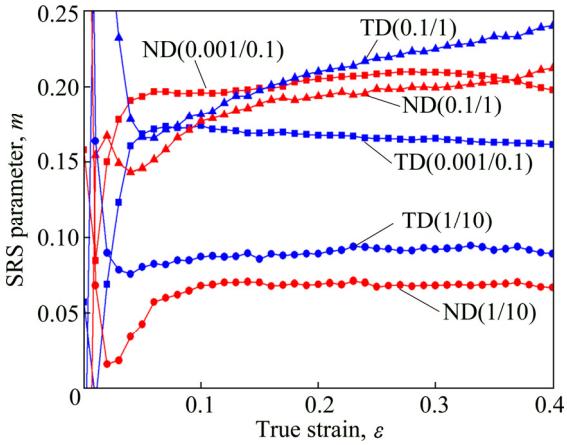

Fig. 3 Strain rate sensitivity (SRS) parameter m computed for ND and TD samples with different strain rate ratios ($\dot{\varepsilon}_1 / \dot{\varepsilon}_2$)

Deformation is accommodated mainly by slip and grain boundary sliding at low strain rate and 700 °C, but for the present crystal plasticity simulation, the entire deformation is simply assumed to be solely accommodated by crystallographic slip. Grain boundary sliding may be seen as a complementary deformation mode, so that the total strain rate would be the sum of grain plastic deformation plus grain boundary sliding. Consequently, the simulated texture may develop faster than the experimental one. It has been observed that during creep, at very low strain rate, cross slip controlled the strain rate sensitivity instead of dislocation slip [7]. Dislocation climb may also be activated during deformation and may be the prevailing restoration mechanism [34].

KASSNER et al [35] reported a similar strain rate sensitivity (n=1/m=6.4) for steady state creep. Because Zr was deformed by a phenomenological five-power-law creep, deformation was attributed to a dislocation climb-controlled mechanism, which has been established for pure metals and Class M alloys. They also observed a power low breakdown for high stress, similar to the present decrease in strain rate sensitivity at high strain rate (so also higher stress). This similarity may however be a coincidence because the present strain rate sensitivity was computed in the work-hardening stage of deformation before extensive recrystallization and steady state.

Via in situ TEM, CAILLARD et al [36] observed a steady and homogeneous dislocation motion in prismatic planes below and above 350 °C in a Zr−1Nb alloy, with few cross-slip in the pyramidal and/or basal planes forming super-jogs that were efficient pinning points. They also observed that these super-jogs moved by glide.

The VPSC model uses the rate sensitive (visco−plastic) Eq. (1), in which the strain rate exponent n=1/m is expected to model the strain rate sensitivity, but when $\dot{\gamma}_0$ and $\dot{\varepsilon}$ are taken almost equal, n can be fixed arbitrarily to relatively low value (n≤20), so that the exponent n loses its physical meaning but allows convergence of the solution [37−39]. It must be noted that an accurate measurement of the strain rate sensitivity m should be done at similar microstructure, for example, via strain rate jump tests. Although m is often evaluated as presently, such evaluation over-estimates m [39]. In the present study, the results showed that at $\dot{\varepsilon} \leq 1\ s^{-1}$, the strain rate sensitivity hardly depended on the sample orientation and strain rate. The computed strain rate sensitivities are very similar at low strain (ε<0.1) because the microstructures are similar; when the strain increases (ε>0.1) recovery and recrystallization happen. So, the microstructure depends on the strain rate, and the computed value for m is unreliable. Consequently, the same strain rate exponent n=6 (consistent with m=0.17) has been fixed for all the slip systems. In crystal plasticity theory, neither cross slip nor dislocation climbing is taken into account, and only the deformation systems are considered (i.e., slip and twinning), so the strain rate sensitivity is assumed to be dislocation glide-controlled.

At high strain rate, the strain rate sensitivity decreased significantly. It will be shown in next section that twinning is more active at $\dot{\varepsilon}=10\ s^{-1}$ than that at $\dot{\varepsilon}<10\ s^{-1}$. This tends to confirm the general observation that twinning is almost rate insensitive [40]. However, the present study considered neither high strain rate deformation nor twinning. Deformation at lower temperature, which included twinning, would be similar with high strain rate deformation, and has been investigated by KNEZEVIC et al [12].

3.2 Deformed microstructure

Figures 4 and 5 show the deformed microstructure and texture at ε=0.4 for the ND and TD compressed

samples, respectively. The microstructure depends on the strain rate, with large amount of twins indentified at $\dot{\varepsilon}$=10 s^{-1}, whereas the amount of twin boundary is negligible at $\dot{\varepsilon}$<1 s^{-1}. Dynamic recrystallization (DRX) is observed. At low strain rate extensive grain boundary migration happened, but at high strain rate nucleation governed, which was evidenced by large amount of small grains presented in necklace around the initial grain boundaries in samples deformed at $\dot{\varepsilon}$≥1 s^{-1}. At low strain rate, e.g., $\dot{\varepsilon}$ =0.001 s^{-1}, the microstructure evolution of this alloy was investigated by LUAN et al [41], who observed extensive DRX in the ND sample at ε=0.2, while DRX was retarded in the TD sample. At ε=0.4, the average grain size (~4 μm) was smaller than the initial grain size (~6 μm), while some subgrain boundaries were still present in many grains, consistent with a DRX process. During DRX, grain nucleation, growth, deformation and recovery happened simultaneously during the plastic deformation. Grain growth happened at low strain rate, and more deformed microstructure and more nuclei were present at high strain rate, which was observed in the samples selected on Figs. 4 and 5. The deformed textures represented on (0001) pole figures are very similar at $\dot{\varepsilon}$≤1 s^{-1}, whereas at $\dot{\varepsilon}$ =10 s^{-1} the texture was slightly affected by twinning. Twinning was not considered in the present study, so the texture formation at $\dot{\varepsilon}$ ≤1 s^{-1} was investigated in the next section.

4 Simulated results

4.1 Extreme cases

At high temperature and low strain rate, zirconium alloys may deform by prismatic, basal, pyramidal ⟨*a*⟩ and pyramidal ⟨*c*+*a*⟩ slips. The kind of strains and crystallographic rotations induced by pyramidal ⟨*a*⟩ slip could also be induced by a combination of basal and prismatic ⟨*a*⟩ slips [42]. However, it appeared that the texture evolution induced by pyramidal ⟨*a*⟩ slip was different from a texture deformed by a combination of basal and prismatic slip, so pyramidal ⟨*a*⟩ slip was also considered. The number of slip modes considered was higher than the number of curves that could be used to determine the material parameters, consequently, many different sets of parameters could reproduce the stress−strain curves, but may fail to reproduce some other behaviors. Many simulations were done in an attempt to determine the CRSS parameters of Eq. (2) that fit the experimental data. When prismatic, basal and pyramidal ⟨*c*+*a*⟩ slip modes were considered, it appeared

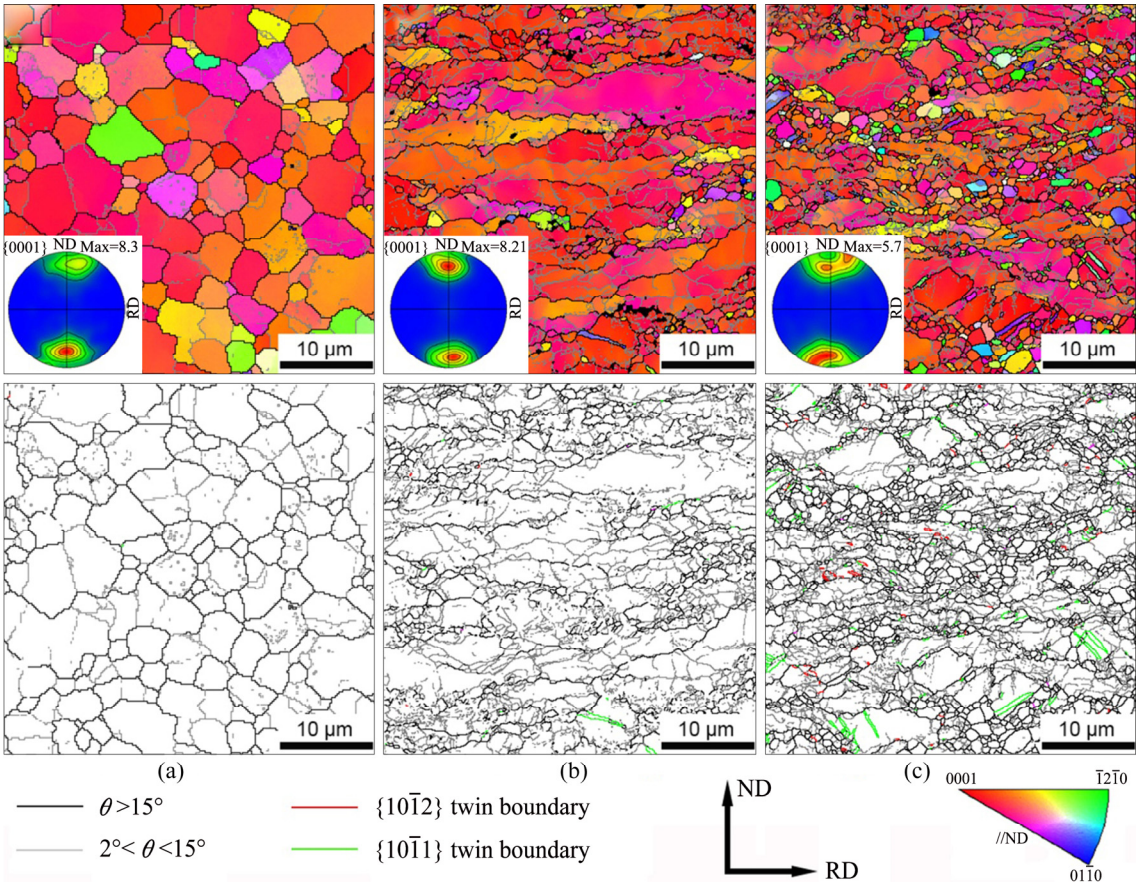

Fig. 4 ND compression IPF maps, boundary maps and (0001) pole figures at ε=0.4 and different strain rates: (a) 0.001 s^{-1}; (b) 1 s^{-1}; (c) 10 s^{-1}

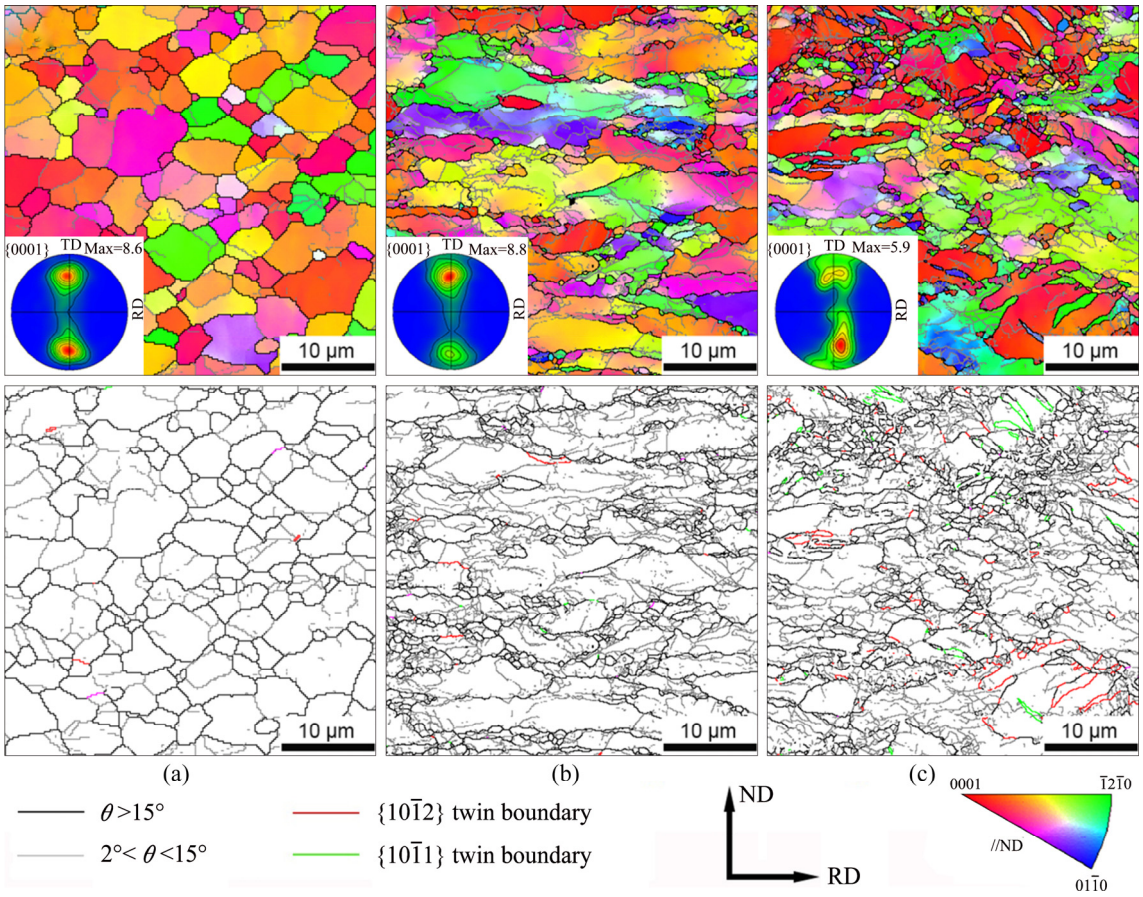

Fig. 5 TD compression IPF maps, boundary maps and (0001) pole figures at ε=0.4 and different strain rates: (a) 0.001 s^{-1}; (b) 1 s^{-1}; (c) 10 s^{-1}

that the main 'variable' was the CRSS for basal slip τ_c^{basal}.

In order to investigate the material parameters able to reproduce the ND and TD compression curves, several cases, based on strong hypothesis and assumptions, were tested and presented in this section. The predicted textures after ND and TD compression tests to ε=0.4 were compared with the experimental ones in Figs. 6 and 7, respectively, and the reliability of the cases was discussed. The simulation was made with the Affine self-consistent (SC) scheme, and for each case considered, different hypotheses and material parameters are summarized in Table 1. The material parameters, i.e., the parameters describing the CRSS evolution for each slip mode, were determined to fit the ND and TD experimental flow stress at $\dot{\varepsilon}$ =1 s^{-1}. Because the experimental strain rate sensitivity m=0.17 was used in Eq. (1), and all the slip modes were assumed to have the same strain rate sensitivity exponent n=6, the simulated deformed textures and anisotropy are independent of the strain rate and all stress−strain curves at $\dot{\varepsilon} \leq 1$ s^{-1} can be reproduced at ε<0.1. At ε>0.1, recovery and DRX are very important at low strain rate, so the material is softer than the predicted. In all cases, prismatic slip was assumed to be the easiest deformation mode, whereas pyramidal ⟨c+a⟩ slip was assumed to be the hardest, which were minimal but reasonable assumptions based on previous studies.

It is interesting to note that in the experiment and all the simulations the {10$\bar{1}$0} //RD (extension direction) fiber predominated in the TD compression samples; the {10$\bar{1}$0} parallel to the extension direction was a signature of prismatic slip [43].

With Cases 1 and 2 (hard basal and pyramidal ⟨a⟩ slip), the predicted textures after ND compression (ND-c) were dramatically different from the experimental one. Experimentally, ND compression gathered the ⟨c⟩ axis at ~25° from the compression direction, whereas high activity for ⟨c+a⟩ slip made the ⟨c⟩ axis rotate toward the extension direction [43] and ⟨c⟩ axis gathered at ~45° from the compression direction, a position at which basal (or pyramidal ⟨a⟩) slip was easily activated.

Case 3 (easy basal slip) reproduced very good ND-c texture; however, after TD compression (TD-c) the ⟨c⟩ axis of grains gathered too closely to the compression direction due to extensive basal slip activity, while a minor texture component ⟨c⟩ parallel to ND remained.

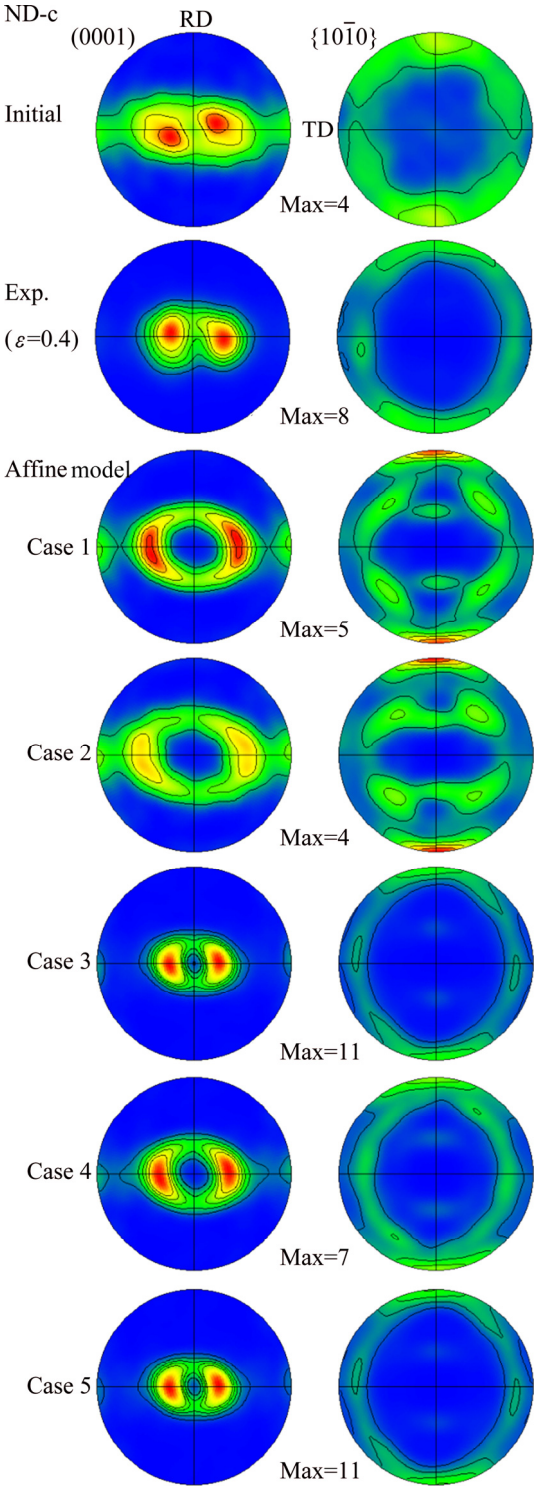

Fig. 6 ND compression (0001) and {10$\bar{1}$0} poles figures of initial, experimental, simulated textures at ε=0.4 with Affine model for Cases 1−5 corresponding to material parameters in Table 1

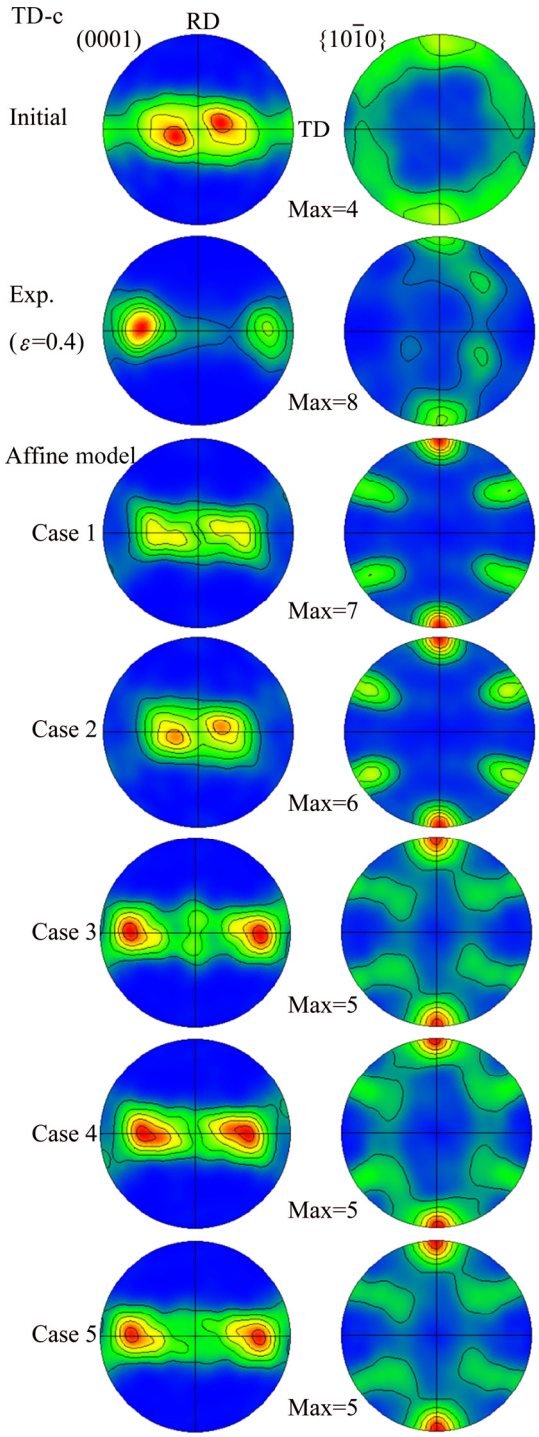

Fig. 7 TD compression (0001) and {10$\bar{1}$0} poles figures of initial, experimental, simulated textures at ε=0.4 with Affine model for Cases 1−5 corresponding to material parameters in Table 1

As for Case 4 (easy pyramidal ⟨a⟩ slip), the ND-c simulated texture had the ⟨c⟩ axis gathered relatively too far from the ND. Simulation of TD-c made the ⟨c⟩ axis spread in the ND−TD plane, but the grains with ⟨c⟩ parallel to TD (compression direction) were expelled.

As for Case 5, during TD-c the ⟨c⟩ axis gathered too closely to the TD direction. The equilibrium position of the ⟨c⟩ axis in respect to the compression direction is dictated by the ratio $\tau_c^{\langle c+a\rangle}/\tau_c^{\text{basal}}$ [42]; lowering this ratio would make ⟨c⟩ tilt far away from the compression direction. Lowering the ratio $\tau_c^{\langle c+a\rangle}/\tau_c^{\text{basal}}$ could make

Table 1 Parameters $\tau_0/\tau_1/\theta_0/\theta_1$ (in MPa) for different cases investigated

Case No.	Hypothesis	Prismatic	Basal	Pyramidal ⟨*a*⟩	Pyramidal ⟨*c*+*a*⟩
1	$\tau^{prism}<\tau^{basal}=\tau^{\langle c+a\rangle}$	10/2/100/18	95/55/300/0	−	95/55/300/0
2	$\tau^{prism}<\tau^{pyr\langle a\rangle}=\tau^{\langle c+a\rangle}$	5/2/100/18	−	85/50/300/0	85/50/300/0
3	$\tau^{prism}=\tau^{basal}<\tau^{\langle c+a\rangle}$	37/22/100/0	37/22/100/0	−	150/25/300/0
4	$\tau^{prism}=\tau^{pyr\langle a\rangle}<\tau^{\langle c+a\rangle}$	32/22/100/5	−	32/22/100/5	125/38/150/0
5	$\tau^{prism}=\tau^{basal}=\tau^{pyr\langle a\rangle}<\tau^{\langle c+a\rangle}$	42/23/80/0	42/23/80/0	42/23/80/0	140/45/300/0

the simulated texture closer to the experimental one. But it is also possible that the simulated texture rotation is faster than the experimental one, because experimentally a part of the strain may be accommodated by grain boundary sliding, or because grain boundary sliding may decrease the rigid body rotation of the grains, which in turn decreased the rotation rate. Simulated textures are systematically stronger than the experimental ones because of the "homogeneous medium" assumption; consequently simulations can only reproduce the texture evolution tendency.

In summary, Case 5, with hypothesis $\tau^{prism}=\tau^{basal}=\tau^{pyr\langle a\rangle}$, predicted the best-fit texture evolution tendency among all the tested extreme cases, whereas Cases 3 and 4 were relatively good.

4.2 Compromise case

The previous section showed that several hypotheses (cases) were excluded, whereas some others resulted in relatively good (but not perfect) deformed texture. In order to use the benefit of both pyramidal ⟨*a*⟩ slip that pushes the ⟨*c*⟩ axis away from TD during TD compression (Case 4) and basal slip that gathers ⟨*c*⟩ close to the compression direction (Case 3), a "compromise case 6" was simulated. The assumed hypothesis was $\tau_c^{prism}<\tau_c^{basal}=\tau_c^{pyr\langle a\rangle}<\tau_c^{\langle a+a\rangle}$ in order to slightly decrease the ratio $\tau_c^{\langle a+a\rangle}/\tau_c^{basal}$ while assuming that τ_c^{prism} was the lowest CRSS. Because Case 5 was pretty good, relatively low τ_c^{basal} and $\tau_c^{pyr\langle a\rangle}$ were chosen. In this section, the effect of the self-consistent (CS) scheme was also evaluated: Case 6 was simulated with Affine, Secant and Tangent schemes. Although the Affine model generally allows to simulate the deformation behavior realistically, some upper- and lower-bound models allow to evaluate the reliability of the simulated results. The determined parameters that could fit both the ND-c and TD-c flow stress curves are listed in Table 2. The simulated curves shown in Fig. 2 are computed using the parameters for Affine scheme in Table 2, but all simulated curves are almost identical. The corresponding simulated textures at strain ε=0.4 are presented in Fig. 8. It can be seen that in order to reproduce the mechanical behavior, different SC schemes required relatively close CRSS. The simulated textures were also relatively similar, except that the Secant scheme gathered the ⟨*c*⟩ axis relatively far from the compression direction. Because both parameters and simulated textures are close with these three SC schemes, we can conclude that the VPSC model is highly reliable, and any crystal plasticity-based model would use similar parameters and predict similar textures.

Table 2 Parameters $\tau_0/\tau_1/\theta_0/\theta_1$ (in MPa) for different self-consistent schemes

SC scheme	Prismatic	Basal and pyramidal ⟨*a*⟩	Pyramidal ⟨*c*+*a*⟩
Affine	40/20/80/0	45/23/80/0	135/45/300/0
Secant	30/25/80/0	35/25/80/0	130/50/300/0
Tangent	40/20/80/0	50/22/80/0	135/45/300/0

The slip system activity is shown in Fig. 9. Instead of the relative slip system activity (expressed in %), the real activity corresponding to a normalized strain increment of ε=1 is shown. To deform a crystal with one slip system whose Schmid factor is 0.5, the necessary theoretic activity is 2; for the present materials the total average activity is ~6 for TD sample and ~7 for the ND sample, so a large amount of slips are necessary to accommodate the deformation (for FCC metals, the real average activity is ~4−5). In both samples, basal slip dominated the deformation, while the prismatic slip activity decreased with the increase of strain. At high strain (ε=0.8), the activity (and the texture) under TD-c is similar to that of ND-c at low strain.

4.3 Parameters validation

The plastic anisotropy can be used to evaluate or validate the material parameters [44,45]. In the present study, the plastic anisotropy (Lankford coefficient or *r*-value) has been simulated for all the cases investigated, but unfortunately it has not been measured systematically. Only one measurement has been done prior microstructural observation, so the accuracy and reliability of the experimental value are disputable.

The *r*-values were defined for ND compression as $r=\varepsilon_{xx}/\varepsilon_{yy}$ and for TD compression as $r=\varepsilon_{xx}/\varepsilon_{zz}$ in Fig. 10. For Cases 1 and 2, $\varepsilon_{yy}\approx0$ in ND-c sample and $\varepsilon_{zz}\approx0$ in TD-c sample, so the *r*-values were virtually infinite; for Case 4 (pyramidal ⟨*a*⟩ slip was considered whereas basal slip was excluded), $r\approx3$ for ND-c sample and $r\approx8$ for

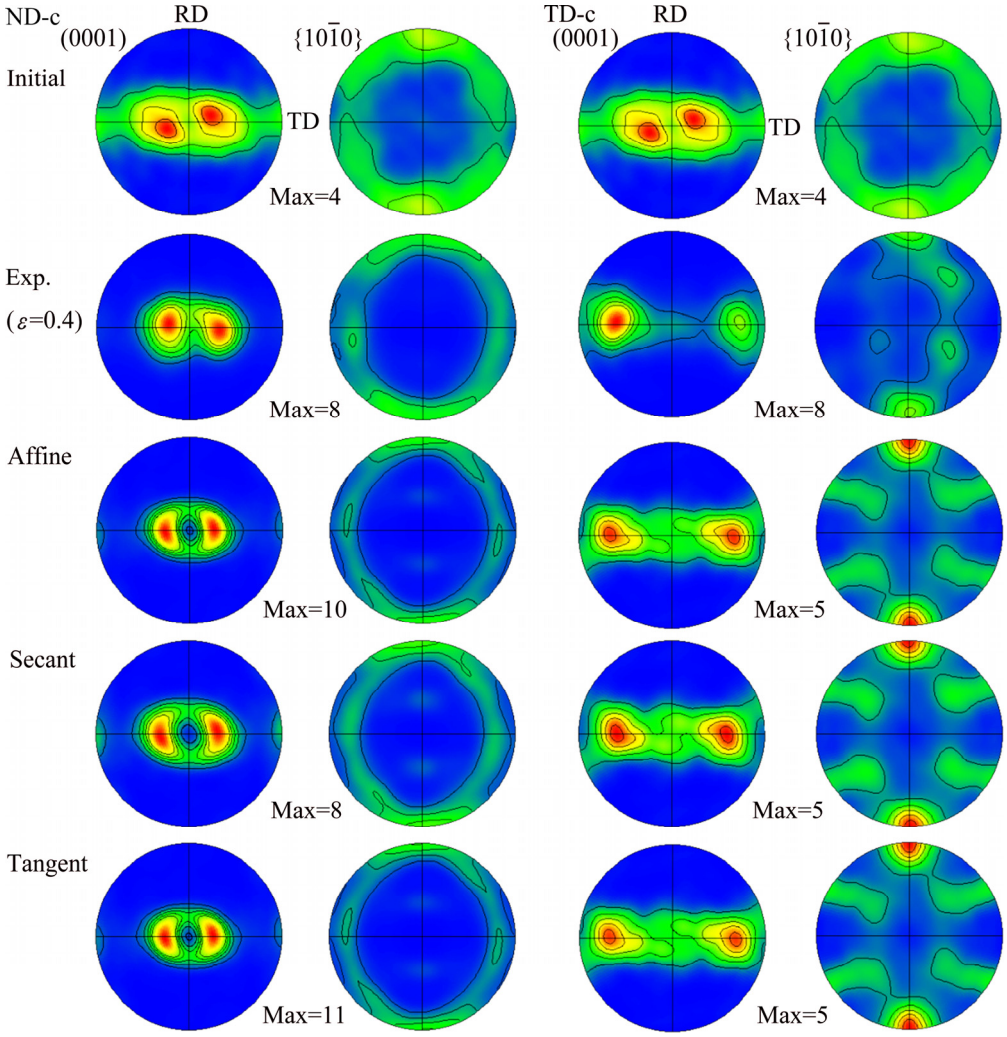

Fig. 8 Simulated ND-c and TD-c textures at ε=0.4 with Affine, Secant and Tangent SC schemes using parameters in Table 2

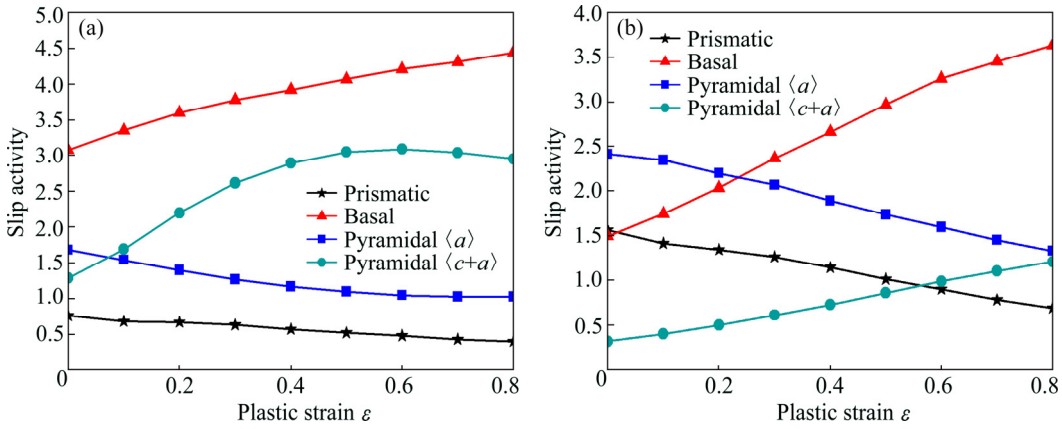

Fig. 9 Slip activity predicted with Affine SC scheme for ND-c (a) and TD-c (b) samples using parameters in Table 2

TD-c sample, which showed that Cases 1, 2 and 4 were unreliable because they definitely could not predict the r-values obtained in the experiments. In regard of the experimental data, the simulation (Case 6-Affine) appeared as a compromise between the acceptable extreme cases and the experimental r-values. We can also note that the predictions show a small difference between the three SC schemes. Keeping in mind that Tangent and Secant SC schemes are the lower- and upper-bound approximations respectively, and Affine is in between, it can be inferred that different SC schemes require relatively close CRSS and also predict relatively close r-values, so the SC schemes are close and reliable.

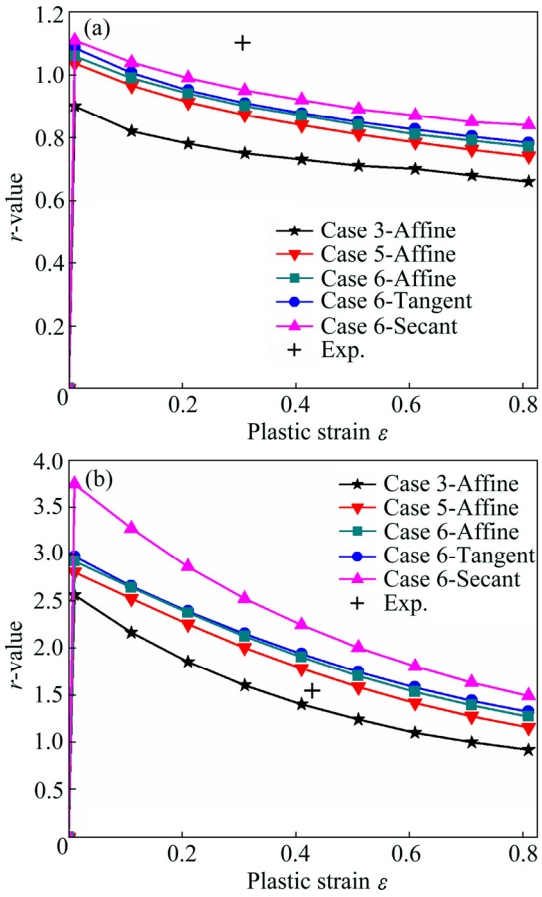

Fig. 10 *r*-values for ND-c (a) and TD-c (b) samples simulated for Cases 3, 5 and 6 with three SC schemes

5 Conclusions

(1) A hot rolled Zr alloy plate was compressed at 700 °C along two directions, and the deformation was investigated via EBSD characterization and VPSC modeling.

(2) At strain rate $\dot{\varepsilon} \leq 1\ s^{-1}$, twinning is hardly activated and the strain rate sensitivity exponent n is 5−6, which seems to be the same for all the slip modes.

(3) Both basal and pyramidal $\langle a \rangle$ slips may be easily activated, with CRSS slightly higher than the one for prismatic slip, while $\langle c+a \rangle$ slip is the harder deformation mode.

(4) The three self-consistent schemes in the VPSC model can fit experimental data with relatively close CRSS values and predict very close results.

Acknowledgments

Thanks go to C. Tomé for sharing the VPSC code.

References

[1] MURTY K L, CHARIT I. Texture development and anisotropic deformation of Zircaloys [J]. Progress in Nuclear Energy, 2006, 48: 325−359.

[2] KRISHNA K V M, SAHOO S K, SAMAJDAR I, NEOGY S, TEWARI R, SRIVASTAVA D, DEY G K, DAS G H, SAIBABA N, BANARJEE S. Microstructural and textural developments during Zircaloy-4 fuel tube fabrication [J]. Journal of Nuclear Materials, 2008, 383(1−2): 78−85.

[3] AKHTAR A, TEGHTSOONIAN A. Plastic deformation of zirconium single crystals [J]. Acta Metallurgica, 1971, 19: 655−663.

[4] ZAEFFERER S. A study of active deformation systems in titanium alloys: Dependence on alloy composition and correlation with deformation texture [J]. Materials Science and Engineering A, 2003, 344: 20−30.

[5] AKHTAR A. Basal slip in zirconium [J]. Acta Metallurgica, 1973, 21: 1−11.

[6] QIAO H, WU P D, WANG H, GHARGHOURI M A, DAYMOND M R. Evaluation of elastic–viscoplastic self-consistent polycrystal plasticity models for zirconium alloys [J]. International Journal of Solids and Structures, 2015, 71: 308−322.

[7] RAUTENBERG M, FEAUGAS X, POQUILLON D, CLOUE J M. Microstructural characterization of creep anisotropy at 673 K in the M5 alloy [J]. Acta Materialia, 2012, 60: 4319−4327.

[8] AKHTAR A. Compression of zirconium single crystals parallel to the *c*-axis [J]. Journal of Nuclear Materials, 1973, 47: 79−86.

[9] MCCABE R J, CERRETA E K, MISRA A, KASCHNER G C, TOME C N. Effects of texture, temperature and strain on the deformation modes of zirconium [J]. Philosophical Magazine A, 2007, 86: 3595−3611.

[10] LEBENSOHN R A, GONZALEZ M I, TOME C N, POCHETTINO A A. Measurement and prediction of texture development during a rolling sequence of Zircaloy-4 tubes [J]. Journal of Nuclear Materials, 1996, 229: 57−64.

[11] BEYERLEIN I J, TOME C N. A dislocation-based constitutive law for pure Zr including temperature effects [J]. International Journal of Plasticity, 2008, 24: 867−895.

[12] KNEZEVIC M, ZECEVIC M, BEYERLEIN I J, BINGERT J F, MCCABE R J. Strain rate and temperature effects on the selection of primary and secondary slip and twinning systems in HCP Zr [J]. Acta Materialia, 2015, 88: 55−73.

[13] YAPICI G G, TOME C N, BEYERLEIN I J, KARAMAN I, VOGEL S C, LIU C. Plastic flow anisotropy of pure zirconium after severe plastic deformation at room temperature [J]. Acta Materialia, 2009, 57: 4855−4865.

[14] GONG J C, BRITTON T B, CUDDIHY M A, DUNNE F P E, WILKINSON A J. $\langle a \rangle$ Prismatic, $\langle a \rangle$ basal, and $\langle c+a \rangle$ slip strengths of commercially pure Zr by micro-cantilever tests [J]. Acta Materialia, 2015, 96: 249−257.

[15] SALEM A A, KALIDINDI S R, SEMIATIN S L. Strain hardening due to deformation twinning in α-titanium: Constitutive relations and crystal-plasticity modeling [J]. Acta Materialia, 2005, 53: 3495−3502.

[16] EVANS C, JONES N G, RUGG D, LINDLEY T C, DYE D. The effect of deformation mechanisms on the high temperature plasticity of Zircaloy-4 [J]. Journal of Nuclear Materials, 2012, 424: 123−131.

[17] HONNIBAL P D, PREUSS M, RUGG D, QUINTA DA FONSECA J. Grain breakup during elevated temperature deformation of an HCP metal [J]. Metallurgical and Materials Transactions A, 2015, 46: 2143−2156.

[18] BARNETT M R, GHADERI A, SABIROV I, HUTCHINSON B. Role of grain boundary sliding in the anisotropy of magnesium alloys [J]. Scripta Materialia, 2009, 61: 277−280.

[19] PEREZ-PRADO M T, RUANO O A. Texture evolution during annealing of magnesium AZ31 alloy [J]. Scripta Materialia, 2002, 46: 149−155.

[20] BOZZOLO N, DEWOBROTO N, GROSDIDIER T, WAGNER F. Texture evolution during grain growth in recrystallized commercially pure titanium [J]. Materials Science and Engineering A, 2005, 397: 346−355.

[21] YI S B, ZAEFFERER S, BROKMEIER H G. Mechanical behaviour

and microstructural evolution of magnesium alloy AZ31 in tension at different temperatures [J]. Materials Science and Engineering A, 2006, 424: 275−281.
[22] GERSPACH F, BOZZOLO N, WAGNER F. About texture stability during primary recrystallization of cold-rolled low alloyed zirconium [J]. Scripta Materialia, 2009, 60: 203−206.
[23] MA Q, LI B, MARIN E B, HORSTEMEYER S J. Twinning-induced dynamic recrystallization in a magnesium alloy extruded at 450 °C [J]. Scripta Materialia, 2011, 65: 823−826.
[24] ISAENKOVA M G, PERLOVICH Y A, FESENKO V A, KRYMSKAYA O A, KRAPIVKA N A, TKHU S S. Regularities of recrystallization of rolled single crystals and polycrystals of zirconium and alloy Zr−1%Nb [J]. The Physics of Metals and Metallography, 2014, 115: 756−764.
[25] WALDE T, RIEDEL H. Modeling texture evolution during hot rolling of magnesium alloy AZ31 [J]. Materials Science and Engineering A, 2007, 443: 277−284.
[26] LEBENSOHN R A, TOMÉ C N. A self-consistent anisotropic approach for the simulation of plastic deformation and texture development of polycrystals: Application to zirconium alloys [J]. Acta Metallurgica et Materialia, 1993, 41: 2611−2624.
[27] KIM M S, JUNG J Y, SONG Y M, CHOI S H. Simulation of microtexture developments in the stir zone of friction stir-welded AZ31 Mg alloys [J]. International Journal of Plasticity, 2017, 94: 24−43.
[28] LUAN B F, ZENG Q H, ZENG W, LIU Q. Dynamic recrystallization of Zr−1Sn−0.3Nb alloy during hot compression [J]. IOP Conference Series: Materials Science and Engineering, 2015, 89: 012034.
[29] KAPOOR R, REDDY G B, SARKAR A. Discontinuous dynamic recrystallization in α-Zr [J]. Materials Science and Engineering A, 2018, 718: 104−110.
[30] SARKAR A, CHANDANSHIVE S A, THOTA M K, KAPOOR R. High temperature deformation behavior of Zr−1Nb alloy [J]. Journal of Alloys and Compounds, 2017, 703: 56−66.
[31] ZENG Q, LUAN B, WANG Y, ZHANG X, LIU R, MURTY K L, LIU Q. Effect of initial orientation on dynamic recrystallization of a zirconium alloy during hot deformation [J]. Materials Characterization, 2018, 145: 444−453.
[32] LUAN B F, GAO S S, CHAI L J, LI X Y, CHAPUIS A, LIU Q. Compression deformation behavior of Zr−1Sn−0.3Nb alloy with different initial orientations at 650 °C [J]. Materials and Design, 2013, 52: 1065−1070.
[33] WANG H, RAEISINIA B, WU P D, AGNEW S R, TOME C N. Evaluation of self-consistent polycrystal plasticity models for magnesium alloy AZ31B sheet [J]. International Journal of Solids and Structures, 2010, 47: 2905−2917.
[34] PEREZ-PRADO M T, BARRABES S R, KASSNER M E, EVANGELISTA E. Dynamic restoration mechanisms in α-zirconium at elevated temperatures [J]. Acta Materialia, 2005, 53: 581−591.
[35] KASSNER M E, PEREZ-PRADO M T, HAYES T A, JIANG L, BARRABES S R, LEE I F. Elevated temperature deformation of Zr to large strains [J]. Journal of Materials Science, 2013, 48: 4492−4500.
[36] CAILLARD D, RAUTENBERG M, FEAUGAS X. Dislocation mechanisms in a zirconium alloy in the high-temperature regime: An in situ TEM investigation [J]. Acta Materialia, 2015, 87: 283−292.
[37] KABIRIAN F, KHAN A S, GNAUPEL-HERLOD T. Visco−plastic modeling of mechanical responses and texture evolution in extruded AZ31 magnesium alloy for various loading conditions [J]. International Journal of Plasticity, 2015, 68: 1−20.
[38] KNEZEVIC M, ZECEVIC M, BEYERLEIN I J, LEBENSOHN R A. A numerical procedure enabling accurate descriptions of strain rate-sensitive flow of polycrystals within crystal visco-plasticity theory [J]. Computational Methods in Applied Mechanics and Engineering, 2016, 308: 468−482.
[39] CHAPUIS A, LIU Q. Effect of strain rate sensitivity in visco-plastic modeling [J]. International Journal of Solids and Structures, 2018, 152−153: 217−227.
[40] KURUKURI S, WORSWICK M J, GHAFFARI TARI D, MISHRA R K, CARTER J T. Rate sensitivity and tension–compression asymmetry in AZ31B magnesium alloy sheet [J]. Philosophical Transactions of the Royal Society A, 2013, 372: 20130216.
[41] LUAN B F, LI X Y, ZHANG M, CHAPUIS A, LIU Q. Deformation mechanisms and dynamic recrystallisation of Zr alloy with different initial textures compressed at 700 ºC [J]. Materials Research Innovation, 2014, 18(S4): s1095−s1101.
[42] AGNEW S R, YOO M H, TOME C N. Application of texture simulation to understanding mechanical behavior of Mg and solid solution alloys containing Li or Y [J]. Acta Materialia, 2001, 49: 4277−4289.
[43] CHAPUIS A, LIU Q. Simulations of texture evolution for HCP metals: Influence of the main slip systems [J]. Computational Materials Science, 2015, 97: 121−126.
[44] JAIN A, AGNEW S R. Modeling the temperature dependent effect of twinning on the behavior of magnesium alloy AZ31B sheet [J]. Materials Science and Engineering A, 2007, 462: 29−36.
[45] ZHOU G W, JAIN M K, WU P D, SHAO Y C, LI D Y, PENG Y H. Experiment and crystal plasticity analysis on plastic deformation of AZ31B Mg alloy sheet under intermediate temperatures: How deformation mechanisms evolve [J]. International Journal of Plasticity, 2016, 79: 19−47.

α-Zr 在 700 °C 下的滑移变形机制

曾庆辉，Adrien CHAPUIS，栾佰峰，刘 庆

重庆大学 材料科学与工程学院，重庆 400044

摘 要：锆合金的力学性能、耐腐蚀性能和吸氢行为与其加工过程中形成的织构密切相关。采用 700 °C 下的压缩变形实验、EBSD 显微组织观察以及黏塑性自洽建模研究 α-Zr 的高温变形行为。结果表明，当应变速率 $\dot{\varepsilon} \leq 1\ s^{-1}$ 时，孪生变形的开启量可以忽略不计。所有滑移系的应变速率敏感因子 m=0.17。选取的材料参数很好地重现了力学各向异性和变形织构，通过对比实验测量与模拟计算得出的应变各向异性对材料参数进行验证。模拟研究结果表明，在高温条件下，柱面滑移是最容易开启的变形机制，而锥面⟨*c*+*a*⟩滑移最难开启，而基面滑移和锥面⟨*a*⟩滑移作为比较容易开启的滑移系在变形中大量开启。

关键词：变形机制；锆合金；EBSD；晶体塑性；塑性变形

(Edited by Wei-ping CHEN)